Performance scaling of a 10-GHz solid-state laser enabling self-referenced CEO frequency detection without amplification

LÉONARD M. KRÜGER,[1,*] **ALINE S. MAYER,**[1] **YOSHITOMO OKAWACHI,**[2] **XINGCHEN JI,**[3] **ALEXANDER KLENNER,**[2] **ADREA R. JOHNSON,**[2] **CARSTEN LANGROCK,**[4] **MARTIN M. FEJER,**[4] **MICHAL LIPSON,**[2,3] **ALEXANDER L. GAETA,**[2,3] **VALENTIN J. WITTWER,**[5] **THOMAS SÜDMEYER,**[5] **CHRISTOPHER R. PHILLIPS,**[1] AND **URSULA KELLER**[1]

[1]*Department of Physics, Institute for Quantum Electronics, ETH Zurich, CH-8093 Zurich, Switzerland*
[2]*Department of Applied Physics and Applied Mathematics, Columbia University, New York, New York 10027, USA*
[3]*Department of Electrical Engineering, Columbia University, New York, New York 10027, USA*
[4]*Edward L. Ginzton Laboratory, Stanford University, California 94305-4085, USA*
[5]*Laboratoire Temps-Fréquence, Université de Neuchâtel, CH-2000 Neuchâtel, Switzerland*
[*]*lkrueger@phys.ethz.ch*

Abstract: A simple and compact straight-cavity laser oscillator incorporating a cascaded quadratic nonlinear crystal and a semiconductor saturable absorber mirror (SESAM) can deliver stable femtosecond modelocking at high pulse repetition rates >10 GHz. In this paper, we experimentally investigate the influence of intracavity dispersion, pump brightness, and cavity design on modelocking with high repetition rates, and use the resulting insights to demonstrate a 10.4-GHz straight-cavity SESAM-modelocked Yb:CALGO laser delivering 108-fs pulses with 812 mW of average output power. This result represents a record-level performance for diode-pumped femtosecond oscillators with repetition rates above 10 GHz. Using the oscillator output without any optical amplification, we demonstrate coherent octave-spanning supercontinuum generation (SCG) in a silicon nitride waveguide. Subsequent f-to-$2f$ interferometry with a periodically poled lithium niobate waveguide enables the detection of a strong carrier-envelope offset (CEO) beat note with a 33-dB signal-to-noise ratio.

1. Introduction

Passively modelocked solid-state lasers generate a coherent train of light pulses evenly spaced in time. In the frequency domain, this corresponds to a frequency comb, where the spacing between two adjacent lines is determined by the pulse repetition rate. Frequency combs are compelling sources for many applications including time-keeping, metrology, and spectroscopy [1–3]. In recent years, significant attention has been placed on compact frequency comb platforms offering larger comb spacings in the range of 1 to 10 GHz with a high power per comb line. Such combs enable high-speed, high signal-to-noise ratio measurements and find application in dual-comb spectroscopy [4–8], microwave photonics [9], telecommunications [10], laser ranging [11,12], astronomical spectrograph calibration [13], and high-speed materials processing [14].

Nowadays, there are several approaches for the generation of multi-gigahertz frequency combs, including passively modelocked ion-doped solid-state lasers [15–21], semiconductor disc lasers [22,23], microresonator combs [24], electro-optic modulator combs [25], and comb-line filtering of megahertz frequency combs [26]. Passively modelocked lasers offer the advantage of

combining high average power with femtosecond pulses and low-noise performance, making them well suited for the above-mentioned applications.

In conventional femtosecond modelocking, stable soliton pulse formation is supported by balancing positive self-phase modulation (SPM) with net anomalous cavity dispersion. At high repetition rates (f_{rep}) however, the low intra-cavity pulse energy makes it increasingly challenging to obtain enough SPM from the weak intrinsic nonlinearities typical of wide band-gap materials [27]. Furthermore, precise dispersion management is complicated by the highly constrained cavity geometry, which only allows for a limited number of optics. In addition, Q-switching instabilities occur at power levels below the threshold for stable continuous-wave (cw) modelocking [28], leading to intensity spikes inside the cavity which can damage optical components. These issues have made it challenging to obtain diode-pumped, watt-level, femtosecond solid-state laser sources at very high repetition rates [29]. To address these issues, we have recently introduced a new type of passively modelocked ultrafast laser based on a simple, self-defocusing straight cavity [30]. A semiconductor saturable absorber mirror (SESAM) is used [31] as a cavity end mirror, while a two-dimensionally patterned quasi-phasematching (QPM) device provides cascaded quadratic nonlinearities to generate a large and negative nonlinear refractive index. The resulting negative SPM enables stable femtosecond soliton modelocking in the normal dispersion regime, despite the low intracavity pulse energies associated with a 10-GHz repetition rate [32].

For most of the frequency comb applications mentioned above, it is necessary to detect and control the two degrees of freedom, *i.e.* the repetition rate f_{rep} and the carrier-envelope offset frequency f_{CEO}. The low pulse energies and limited peak power, inherent in high repetition rate lasers, make it challenging to generate sufficient nonlinear spectral broadening for self-referenced f_{CEO}-detection. In our initial implementation of the straight-cavtiy architecture described above [30], the peak power and pulse duration was limited by several subtle trade-offs between competing intracavity nonlinear processes. The shortest pulses achieved in this configuration (166 fs, 7-nm optical bandwidth) were not sufficient to drive coherent octave-spanning supercontinuum generation (SCG), even when combined with our newest generation of highly efficient dispersion-engineered Si_3N_4 waveguides [33,23].

Here, we present the experimental study on the design space of this laser architecture that was necessary to identify and overcome the critical bottlenecks. In particular, performance scaling to higher output powers was achieved via pumping with a higher brightness, while shorter pulse durations were enabled by designing new dispersion-optimized dichroic output-coupling cavity mirrors. The new laser configuration generates 108-fs pulses with an 11.6-nm-wide optical spectrum centered at 1041 nm and an average output power of 812 mW. The broader laser output spectrum now enables the generation of a coherent octave-spanning supercontinuum and subsequent detection of the carrier-envelope offset (CEO) frequency without the need for external pulse amplification or separate nonlinear compression. We demonstrate supercontinuum generation (SCG) in a Si_3N_4 waveguide with only 48-pJ incident pulse energy in free space before the waveguide (500-mW average power). The SCG device is optimized for f-to-$2f$ interferometry by delivering distinct dispersive-wave peaks spaced one octave apart. Since the energy in these peaks is still limited due to our high repetition rate, we perform second-harmonic generation (SHG) in a reverse proton-exchange (RPE) periodically poled lithium niobate (PPLN) waveguide [34] for f_{CEO} detection via f-to-$2f$. The resulting self-referenced f_{CEO} signal of the free-running laser has a high signal-to-noise ratio (SNR) of 33 dB measured with a resolution bandwidth of 100 kHz. Hence, combining these two waveguide technologies yields an ultra-low pulse energy platform for f_{CEO} detection. Our results represent an important step for high repetition rate and high power per comb line OFC systems based on diode-pumped solid-state lasers (DPSSLs).

2. Laser design and performance scaling

The laser cavity, depicted in Fig. 1, consists of four elements: a curved end mirror with a multi-functional thin-film coating, an ytterbium-doped CaGdAlO$_4$ crystal (Yb:CALGO), a PPLN crystal, and a SESAM. The laser is pumped by a spatially multimode laser diode at 980 nm.
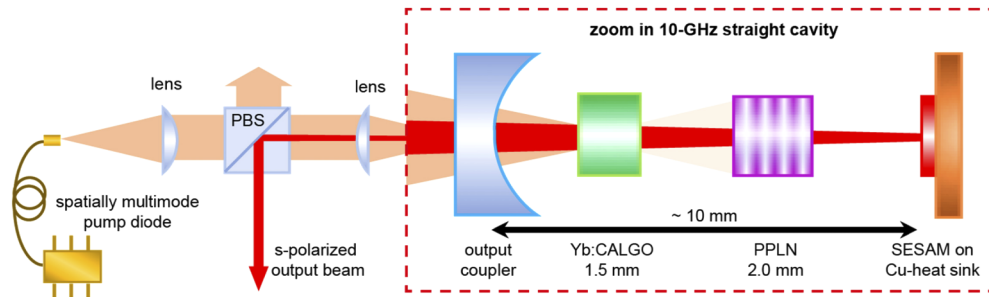

Fig. 1. Illustration of the 10-GHz cavity containing a curved output coupler mirror, Yb:CALGO gain crystal, PPLN, and SESAM. A polarizing beam splitter (PBS) is used to couple the linearly polarized light out of the cavity.

A detailed description of the interplay between the cavity elements and different tradeoffs involved in this new type of straight-cavity laser architecture is given in Appendix A.

2.1. PPLN crystal for self-defocusing laser cavity

While the Yb:CALGO laser crystal offers a broad gain bandwidth [35], its positive nonlinear refractive index also causes a self-focusing Kerr-lens effect. In a standard two-mirror straight-cavity laser configuration, this self-focusing causes the laser beam size on the SESAM to decrease. This effect can lead to damage caused by the high-energy pulses generated in the Q-switched instability regime which is traversed before reaching cw modelocking [28]. In our straight-cavity design, this self-focusing effect is counter-balanced by a self-defocusing of the beam in the PPLN crystal providing a negative nonlinear refractive index n_2. Consequently, an increasing intracavity intensity will cause a stronger defocusing lens, which increases the intracavity beam size and thereby clamps the intensity below the damage threshold of the cavity components [29,30].

Negative nonlinear refraction (negative n_2) effects are not usually supported by the intrinsic third-order electronic nonlinear susceptibility, except at wavelengths near the band edge where two-photon absorption also occurs and leads to high losses [27]. An alternative physical mechanism is therefore required to obtain a negative n_2. Here, we obtain a negative n_2 via phase-mismatched second-harmonic generation (SHG), which is often referred to as cascaded quadratic nonlinearities (CQN) [36]. To implement this process, we use a PPLN crystal with the same two-dimensional QPM design as in Ref. [32]. The available QPM grating k-vector $K_g = (2\pi/\text{period})$ can be tuned from 854 mm^{-1} to 934 mm^{-1}. Note that phase-matched SHG for 1045 nm occurs in MgO:LiNbO$_3$ at a k-vector of 953 mm^{-1} [37].

2.2. Output coupler: dichroic optic with optimized dispersion and curvature

The use of a straight laser cavity containing only two mirrors is very practical when dealing with repetition rates of 10 GHz and higher due to the limited available space. However, since the SESAM acts as one of the end mirrors, the remaining dielectric mirror has to support several core functionalities at once:

- 980-nm pump transmission

- 1030 nm – 1060 nm laser out-coupling

- Laser dispersion management

- Formation of a stable cavity mode via a suitable mirror curvature

The curvature of this mirror, as well as the relative positions of the different elements within the cavity, determine the beam waist at each of these elements and hence have an important influence on the laser performance. In the first phase of this work, we have investigated three different radii of curvature for the dielectric mirror; the details of this investigation are presented in Appendix B. A 12-mm radius of curvature yields the best modelocking performance and is hence used for all further configurations.

All the 10-GHz straight cavity laser configurations presented here operate with a net positive intracavity group delay dispersion (GDD), with positive GDD provided by the material dispersion of the Yb:CALGO and PPLN crystals. However, within the laser regime of soliton modelocking, smaller absolute values of the cavity GDD enable shorter pulses for a given power [38]. Therefore, we have designed output coupler coatings for negative GDD to reduce the total round-trip GDD of the laser cavity. The coatings have a layer structure designed for dispersion compensation using a combination of Gires-Tournois interferometer-type (GTI) and chirped mirror-type design strategies. The optimized thin-film coatings are deposited by ion beam sputtering to minimize residual absorption and scattering. These mirrors are described in Section 2.4 in the context of laser performance optimization.

2.3. *Higher power and improved efficiency via pump brightness improvement*

An advantage of ytterbium-doped gain materials is that they can be pumped with low-cost and efficient multimode fiber-coupled laser diodes at wavelengths around 980 nm. However, to enforce lasing in the fundamental Gaussian mode (TEM_{00}), the ratio of pump to laser spot size must be sufficiently small throughout the laser crystal.

In our earlier work [30], we used a moderate-brightness laser diode (Lissotschenko Mikrooptik GmbH, LIMO, max. 60 W), which had a measured M^2=36 associated with delivery through a 100-μm-diameter, 0.22-NA fiber. The pump beam was focused to a 54-μm $1/e^2$ radius in the center of the gain crystal, while the fundamental TEM_{00}-laser mode radius ($1/e^2$) was 64 μm. However, due to the large M^2, the pump beam diameter would already be nearly 200-μm wide at both ends of the 1.5-mm-long gain crystal (Fig. 2(a)). As a consequence, we observed the onset of higher-order transverse laser modes at high pump powers, which deteriorated the laser output beam quality for output powers > 1.2 W.

Here, we use a new diode (BWT-bj) to address this issue: it delivers up to 20 W of average power through a 105-μm-diameter, 0.15-NA fiber and has an M^2 of 17 (measured with a Thorlabs BP104-IR beam profiler). The diode incorporates a volume Bragg grating for wavelength stabilization, leading to a narrow optical bandwidth of 0.6 nm full width at half maximum (FWHM) around a center wavelength of 980 nm. We stabilize the temperature to 40.5°C such that the diode gain at operating power overlaps with the VBG center wavelength. The lower divergence of the BWT diode leads to a better spatial overlap of the pump and fundamental laser mode inside the gain crystal compared to the LIMO diode (Fig. 2(a)).

With this new diode, the slope efficiency in cw-modelocking was 1.4 times higher (29% instead of 21%), and the maximum average output power was 1.2 times higher (Fig. 2(b)) compared to the laser presented in [30]. For these efficiency measurements, we keep all the laser cavity components the same as in [30]. To the best of our knowledge, the new result (1.44 W with pulse duration of 172 fs and a center wavelength of 1051 nm) represents the highest average power of all diode-pumped laser oscillators with a repetition rate above 10 GHz.
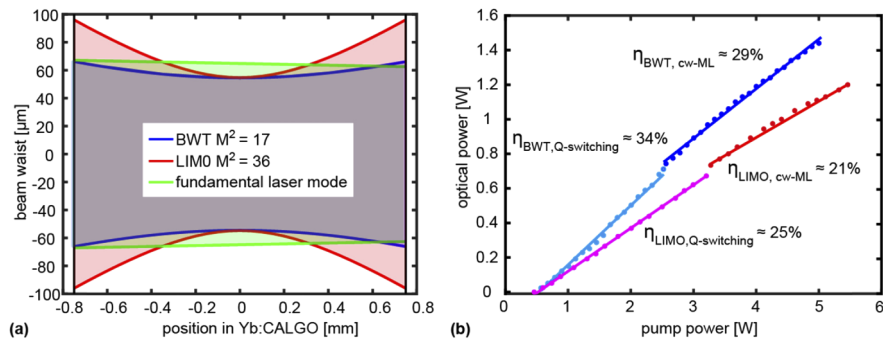
Fig. 2. (a) Calculate transverse beam width of the focused multimode pump and fundamental laser mode inside the 1.5-mm-long Yb:CALGO crystal. The calculation assumes the second-order moment calculation of [39] together with the measured M^2 values. (b) Optical output power as a function of pump power. The lower divergence of the new pump diode supports a higher slope efficiency for both cw-modelocking (cw-ML) and below the cw-modelocking threshold, where Q-switching instabilities occur.

2.4. Pulse duration shortening via intracavity dispersion optimization

As shown in Ref. [30], the negative SPM from the PPLN is sufficient to achieve soliton modelocking using only the bulk-material GDD of the intracavity crystals, *i.e.* with the signs of SPM and GDD both inverted compared to conventional soliton formation. However, the cavity GDD becomes an important parameter when optimizing pulse duration. Therefore, we measured the GDD of the mirrors with a home-built white-light interferometer. The interferometer is designed for flat mirrors, and therefore we measured the GDD of flat mirrors which were coated in the same run as the curved mirrors used in the laser.

For our earlier results, we used a low-GDD commercial output coupling mirror with a GDD of 0 fs^2 at 1030 nm. As can be seen from Fig. 3(a) (blue curve), this mirror was not particularly optimized to provide a flat GDD over a large bandwidth. Hence, we designed two new mirrors with the same radius of curvature (12 mm), very similar transmission properties at the pump and laser wavelengths (Figs. 3(b) and 3(c)), but GDD values of −360 fs^2 at 1042 nm and −870 fs^2 at 1041 nm, respectively (Fig. 3(a), green and red curves). Care was also taken to flatten the GDD profile over the wavelength range of interest, i.e. 1020-1060 nm. Note that the Yb:CALGO and PPLN crystals provide approximately +1280 fs^2 per cavity round-trip in total.
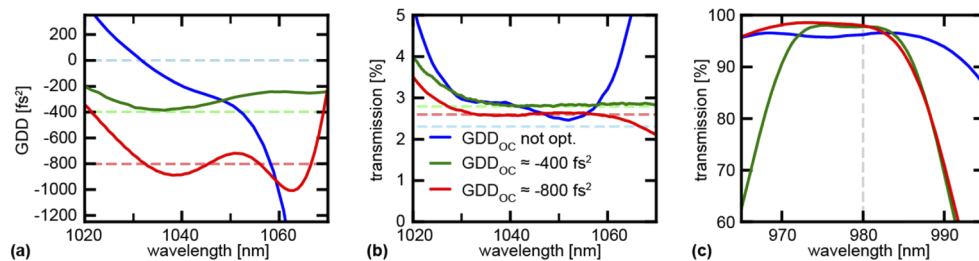

Fig. 3. Characterization of the three output couplers: (a) measured GDD (b) output coupler transmission and (c) pump transmission.

We have characterized and optimized the modelocking behavior for the three different mirror configurations. The transverse position of the PPLN crystal, and therefore the phase mismatch, was adapted for each configuration in order to obtain the shortest pulses at the highest possible

output powers. The proximity to phase matching influences the achievable laser performance in several ways. Operating closer to phase matching results in a stronger nonlinear refractive index, which yields more SPM and a stronger self-defocusing effect (clamping the intensity on the SESAM during Q-switching). A smaller phase mismatch also leads to a lower amount of parasitic SHG from the random duty-cycle errors in the QPM structure [40] for a given amount of cascading-induced SPM. On the other hand, if the phase mismatch at the center wavelength is too small, the wings of the optical spectrum can satisfy phase matching, leading to increased SHG losses which the QPM grating apodization structure cannot sufficiently suppress [32]. Based on these considerations, the phase mismatch must be increased in order to achieve shorter pulses due to the larger optical bandwidth required. However, this also reduces the value of n_2, which means that (i) less overall SPM is available, and (ii) for a given SPM, there is more parasitic SHG in the crystal. To address these issues, the magnitude of the cavity GDD can be decreased, such that less SPM is needed for soliton formation.

We measured the optimal laser performance achieved with the three different mirror configurations. The results are summarized in Table 1; to the best of our knowledge, the values highlighted in bold represent record levels for >10 GHz DPSSLs.

Table 1. Summary of different laser configuration tested to achieve shorter pulse durations.

Laser parameters	Configuration 1	Configuration 2	Configuration 3
Output coupling rate	2.5%	2.8%	2.6%
Output coupler GDD (GDD_{OC})	Significant GDD slope	$-360fs^2$	$-870fs^2$
Total GDD at laser wavelength	$+930fs^2$	$+920fs^2$	$+410fs^2$
PPLN grating vector K_g	888.4 mm^{-1}	914.8 mm^{-1}	910.0 mm^{-1}
Repetition rate f_{rep}	10.52 GHz	10.45 GHz	10.40 GHz
Cw-modelocking threshold	740 mW	410 mW	300 mW
Maximum average power P_{avg}	**1.44 W**	1.18 W	812 mW
Pulse duration τ_p	172 fs	149 fs	**108 fs**
Laser center wavelength λ_0	1051 nm	1042 nm	1041 nm
Spectral bandwidth (FWHM) $\Delta\lambda$	7.1 nm	8 nm	11.6 nm
Self-frequency shift	-4 nm/W	-7 nm/W	-13 nm/W
Modelocking slope efficiency	29%	27%	27%

The laser configuration with the commercial output coupler (indicated in blue in Fig. 4 and blue text in Table 1) has a positive net intracavity dispersion of $+930$ fs^2 per cavity round-trip at the center laser wavelength of 1051 nm and a transverse position in the fan-out PPLN crystal corresponding to a grating vector of $K_g = 888.4$ mm^{-1}. We achieve a maximum output power of 1.44 W, with pulses of 172 fs and a spectrum featuring a FWHM of 7.1 nm centered at 1051 nm; this is the configuration previously presented in Section 2.3. The spectrum is slightly asymmetric and the peak shifts by approximately -4 nm/W due to a self-frequency shift (SFS) effect (see description in Appendix B).

The net intracavity dispersion in a second laser configuration (green curves in Fig. 4) is reduced to $+920$ fs^2 at the laser wavelength of 1042 nm by a curved mirror with a dispersion compensating coating of -360 fs^2. An increased sensitivity with respect to Q-switching instabilities requires a stronger nonlinear defocusing lens in order to protect the cavity elements from damage. Optimal operation is found with a grating vector of $K_g = 914.8$ mm^{-1}. The reduced intracavity dispersion and much lower dispersion slope leads to shorter pulses of 149 fs at 1.18 W with a FWHM of 8 nm at a center wavelength of 1042 nm. The observed SFS of the peak wavelength is -7 nm/W.

We achieve the shortest pulses in a third configuration (red curves in Fig. 4) with a net cavity dispersion of only $+410$ fs^2 at 1041 nm with a -870 fs^2 dispersion compensation curved mirror
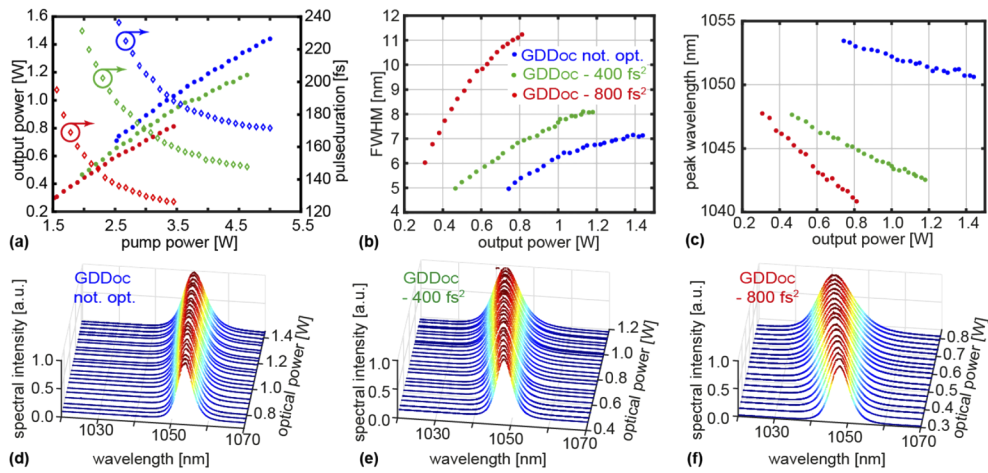
Fig. 4. (a) Output power (left axis) and pulse duration (right axis) for the three laser configurations with total of $+930\,\text{fs}^2$ (blue), $+920\,\text{fs}^2$ (green) and $+410\,\text{fs}^2$ (red) intra-cavity dispersion. The pulse duration decreases with increasing output power, which is indicative of a soliton pulse shaping mechanism. (b) FWHM of the optical spectrum for the three laser configurations. The increase with pump power is not linear (as would be expected for normal soliton modelocking) but shows a saturation, linked to the wavelength dependent nonlinear losses introduced by the cascading process. (c) The peak wavelength shifts towards shorter wavelength with increasing output power, again linked to the cascading process discussed in Section 4. (d)-(f) Measured optical spectrum evolution for the configuration without dispersion management, $-360\,\text{fs}^2$ and $-870\,\text{fs}^2$ GDD$_{OC}$, respectively.
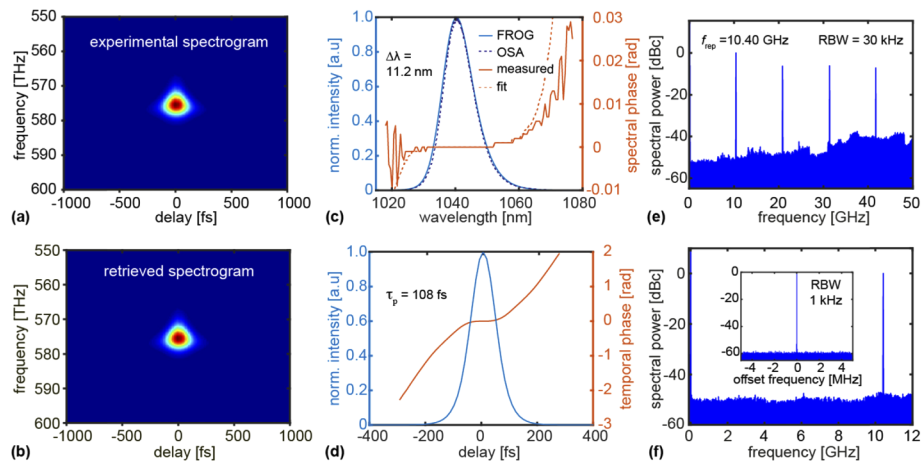

Fig. 5. Modelocking characterization at 812-mW average output power and 108-fs pulses:(a) measured and (b) retrieved FROG spectrograms. (c) Optical spectrum; retrieved FROG trace (solid line) and spectrum measured with an optical spectrum analyzer (dotted line) overlap and indicate a FWHM of 11.6 nm. The retrieved phase indicates transform-limited pulses with a flat phase across the pulse spectrum. (d) Retrieved FROG temporal intensity indicating a pulse duration of 108 fs and a flat temporal phase. (e) Microwave spectrum showing the first four harmonics (f) zoom around the first harmonic show a high signal-to-noise ratio > 60 dB for the peak corresponding to the pulse repetition rate of 10.40 GHz.

and a grating vector of $K_g = 910.0$ mm^{-1}. We obtain a maximum output power of 812 mW with a corresponding pulse duration of 108 fs after compensating for the dispersion of the PBS (see Fig. 1). The spectrum has a FWHM of 11.6 nm centered at 1041 nm and the repetition rate is 10.40 GHz. We observe a strong SFS of −13 nm/W. In Fig. 5, we show the characterization of this configuration. The pulse duration was measured by frequency resolved optical gating (SHG FROG). To the best of our knowledge, this result represents the shortest pulse duration from a directly diode-pumped laser with repetition rates above 10 GHz.

By longitudinal translation of the SESAM we can tune the repetition rate from 10.2 GHz to 10.8 GHz. Within this range, there exist instabilities at a few discrete repetition rate values, indicated by beam deteriorations and fluctuations in average output power. These instabilities are caused by an increased coupling to higher spatial modes, which occurs near modal degeneracy points of the laser cavity [41,42]. For further experiments, the repetition rate was adjusted to 10.5 GHz.

3. Self-referenced f_{CEO} detection

The short-pulse laser configuration is used for subsequent self-referenced f_{CEO} detection. The emitted laser pulses were coupled into a dispersion-engineered Si$_3$N$_4$ ridge waveguide to generate a supercontinuum (SC) with dispersive waves around 720 nm and 1440 nm. The waveguide, illustrated in Fig. 6(a), has a cross section of 740 nm (width) × 720 nm (height) and a length of 50 mm [23]. The waveguide facets are uncoated. An overall device throughput of 38% is achieved, *i.e.* the ratio of power measured after the lens collimating the waveguide output and the power measured before the coupling lens into the waveguide. The average power incident on the waveguide is adjusted to 500 mW (48 pJ pulse energy) in order to maximize the SNR in the subsequent f-to-2f interferometer.
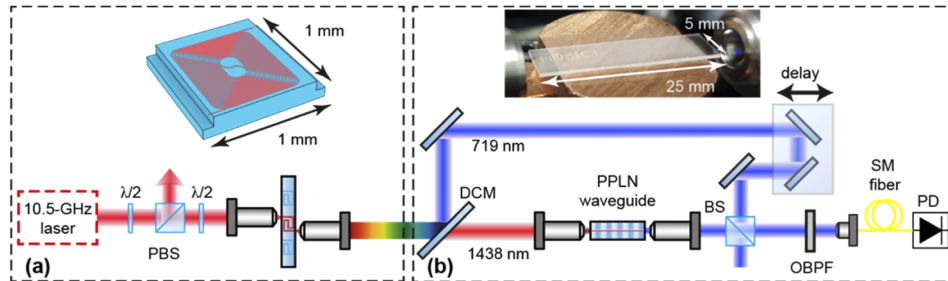

Fig. 6. Low-pulse-energy platform for self-referenced f_{CEO} detection. (a) Efficient SCG in dispersion-engineered Si$_3$N$_4$ waveguide. (b) f-to-2f interferometry including an RPE PPLN waveguide for efficient SHG. The SC is split by a dichroic mirror. The long wavelength component at 1438 nm is coupled into a PPLN waveguide and recombined with the short wavelength component of the SC at 719 nm in a 50:50 beam splitter (BS). The combined signals pass a 10-nm-wide bandpass filter (OBPF) before being coupled into a single-mode (SM) fiber and sent to the photodetector.

The generated SC is collimated and split by a dichroic mirror (Thorlabs DLMP1000). The long wavelength part is additionally long-pass filtered (Thorlabs LP1200) and coupled into a PPLN waveguide. The total throughput of the waveguide (collimated free-space output to collimated free-space input) is 28%. The short-wavelength component of the SC and the frequency-doubled light from the PPLN waveguide are combined with a cube beam-splitter (BS) and coupled into a single-mode fiber to optimize mode matching of the two beams and decouple the delay from spatial overlap. In Fig. 7(b), we show the combined and bandpass-filtered spectrum after the fiber. On the peak of the spectrum, we have an optical power density of ~15 µW/comb-line.
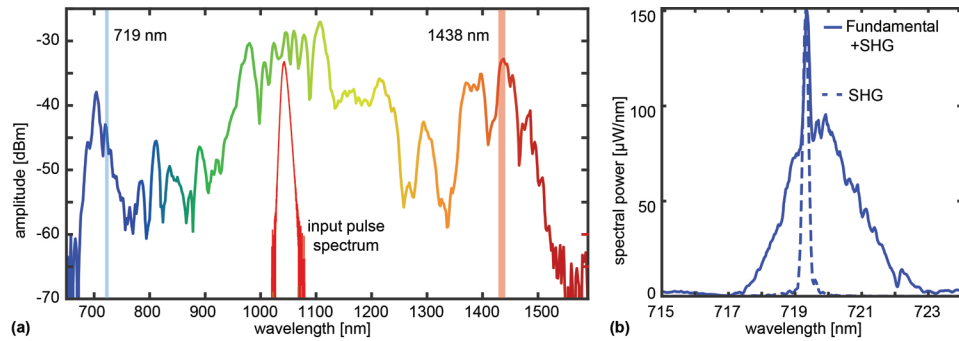
Fig. 7. (a) 10.5-GHz octave spanning SC generated in a Si_3N_4 waveguide with 115-fs input pulses (read line) and 500 mW of incident average power. The spectral components around 1438 nm (red vertical shaded) and 719 nm (blue vertical shaded) were used for f-to-$2f$ interferometry (b) The short-wavelength component of the SC was overlapped with the frequency-doubled long-wavelength component around 719 nm (blue dashed line) in a single-mode fiber.

The fiber is plugged into a fiber-coupled 25-GHz InGaAs photodiode (Newport 1434), whose output is sent through a 25-dB voltage amplifier and connected to a microwave spectrum analyzer. Figure 8(a) shows the CEO beat notes detected with a 33-dB SNR and a short-term linewidth of 6 MHz measured with a resolution bandwidth of 100 kHz. In this free-running mode, the drift amounts to ~250 MHz over 20 minutes. Modulating the pump power manually reveals a remarkably linear tuning behavior of f_{CEO} from zero up to f_{rep} (Fig. 8(b)) (small jumps correlate with the output current precision of the diode driver used (Delta Elektonica SM 18-50). This measurement represents the first f_{CEO} detection from an unamplified Yb-based oscillator with a repetition rate exceeding 10 GHz. A systematic study and optimization of the noise contributions from mechanical, optical, electronic and other sources will be required in order to substantially reduce the laser's free-running noise and thereby enable full comb stabilization with low residual noise in the future.
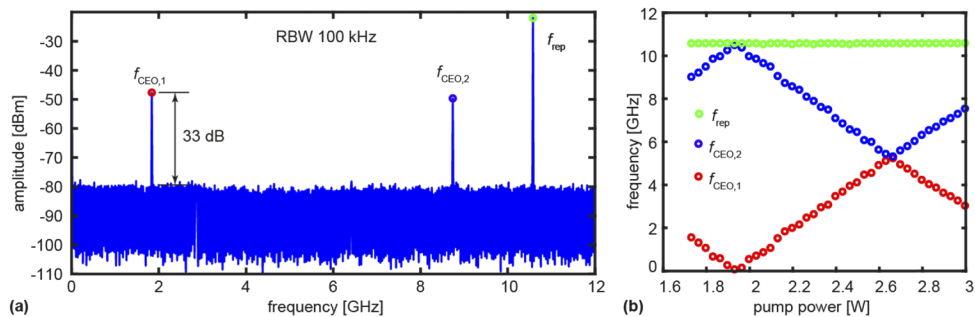

Fig. 8. (a) RF spectrum detected with a fiber- coupled 25-GHz InGaAs detector. Two strong beat notes with 33-dB SNR are symmetrically located with respect to $f_{rep}/2$. (b) Lower frequency beat note $f_{CEO,1}$ (red circle), higher frequency beat note $f_{CEO,2}$ (blue circle) and f_{rep} (green circle) are measured for optical pump powers of 1.7 W to 3 W; see Fig. 4(a) for the corresponding laser output power in the laser configuration used for this measurement.

4. Conclusion

In this paper, we have presented a detailed experimental modelocking study of a straight-cavity architecture that led to the first self-referenced carrier-envelope offset frequency detection of a diode pumped solid state laser with a repetition rate above 10-GHz.

In a first part, we have shown significant pulse shortening due to reduced intracavity dispersion, achieved with dispersion-compensating output coupler coatings. We obtain new record-level performance for diode-pumped femtosecond oscillators with repetition rates above 10 GHz: the highest power (1.44 W, 172 fs) and shortest pulses (108 fs, 812 mW). Moreover, we have observed and characterized a self-frequency shift towards shorter wavelength with increasing pump power, caused by the presence of group velocity mismatch (GVM) between the fundamental and second-harmonic in the cascading process. We identify this GVM as the main factor limiting the laser performance; it may however be improved by using a material platform with a smaller GVM.

In a second part, we have used the short-pulse laser configuration, emitting pulses at a pulse repetition rate of 10.5 GHz with an optical spectrum up to 11.6 nm and pulse energy of 77 pJ, to generate a coherent octave-spanning supercontinuum in a dispersion-engineered Si_3N_4 waveguide. Moreover, an RPE PPLN waveguide is used for efficient SHG, allowing for self-referenced f_{CEO} detection in an f-to-$2f$ interferometer with a 33-dB signal-to-noise ratio over a large range of output powers. This result represents an important milestone for compact optical frequency combs from DPSSLs with multi-gigahertz line spacing and high power per comb-line.

Appendix A: Overview of the laser building blocks and their interaction

The primary role of the four cavity components depicted in Fig. 1 are illustrated in Fig. 9 and their detailed properties will be reviewed in the subsections following below.
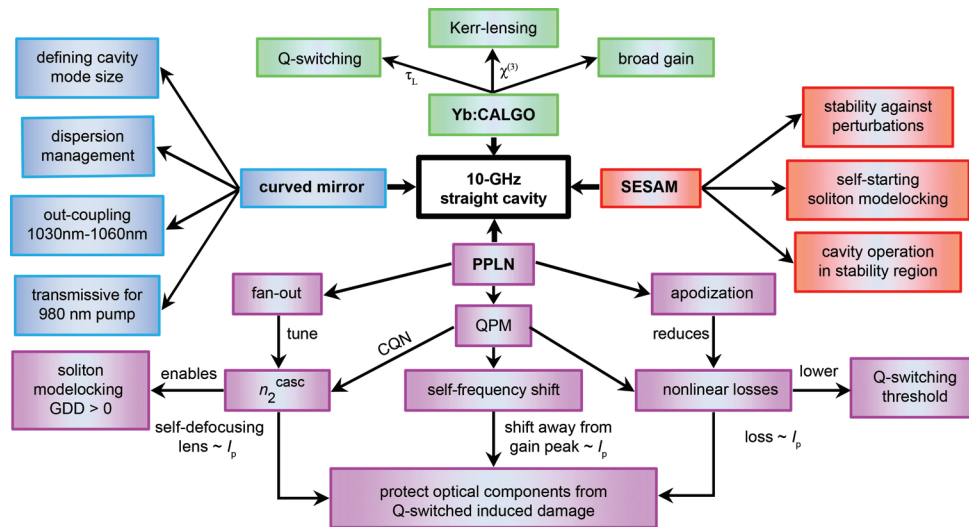

Fig. 9. Spider-web illustrating the interplay between various effects in the 10-GHz straight cavity laser. A curved mirror (blue shaded, left part) and a SESAM (red shaded, right part) form a straight cavity. A Yb:CALGO gain crystal (green shaded, top part) offers broad gain to support 100-fs-short pulses. Its long upper-state lifetime ($\tau_L \approx 420$ μs) gives rise to Q-switching instabilities. The third-order susceptibility ($\chi^{(3)}$) causes a self-focusing Kerr lens, which is compensated by a self-defocusing lens generated by cascaded quadratic nonlinearities (CQN) in the PPLN device (purple shaded, bottom part), enabling stable cw-modelocking.

PPLN

The PPLN crystal plays a crucial role in the straight cavity laser architecture:

- It has a large nonlinear refractive index n_2^{casc}, supporting strong soliton pulse shaping effects at low (few-nJ) intracavity pulse energies.

- The corresponding SPM is negative, allowing soliton formation with net positive round-trip cavity GDD.

- The negative SPM also enables a self-defocusing cavity, with increasing beam sizes on the intracavity components with respect to laser peak power.

- The crystal has a fan-out QPM structure which allows the QPM period, and hence the effective n_2^{casc}, to be continuously tuned by translation of the crystal. We made use of this feature in each experimental configuration presented below to optimize the performance and avoid Q-switching-related damage effects.

- It has an apodized QPM structure [32], which helps suppressing SHG losses that can preclude modelocking if they are too large.

- Group velocity mismatch (GVM) between the fundamental wave and second-harmonic in the CQN process leads to a self-frequency shift effect [43]. In our laser, this tends to cause the laser wavelength to shift away from the gain peak, which also helps to clamp the intracavity intensity.

SESAM

Self-starting and stable modelocking is achieved via a SESAM used as the flat end-mirror of the straight cavity. Suitable SESAM parameters are crucial for the laser performance. The parameters of the SESAM used for the 10-GHz cavity are listed in Table 2. We use a temperature controller (Thorlabs TED 4015) in combination with a water-cooled Peltier mount to stabilize the SESAM temperature. The temperature-stabilization was required to maintain a constant modulation depth, which is essential to obtain reliable self-starting modelocking: if the temperature is not stabilized, heating will cause the quantum well absorption to slightly shift towards longer wavelengths [44]. This shift increases the modulation depth and hence increases the amount of energy absorbed during Q-switching instabilities, which can ultimately result in damaged spots. On the other hand, cooling the SESAM too much reduces the modulation depth to the point where it becomes insufficient to initiate fundamental cw-modelocking. We observed that when stabilizing the SESAM temperature such that $\Delta R < 1\%$, no damage occurred, but also no transition from Q-switching instabilities to stable cw-modelocking operation would be initiated anymore. We thus experimentally determined the optimum temperature for this particular SESAM to be 13 °C.

Table 2. Summary of the SESAM parameters used in the 10 - GHz straight-cavity laser.

SESAM Parameter	
Distributed Bragg mirror	30 pairs of GaAs/AlAs
Absorber	Single InGaAs quantum well embedded in AlAs
Saturation fluence F_{sat}	8 µJ/cm^2
Inverse saturable absorption coefficient F_2	500 mJ/cm^2
Modulation depth ΔR	1%
Nonsaturable losses ΔR_{ns}	0.12%

Gain crystal

In recent years, Yb:CaGdAlO$_4$ has been explored extensively due to its low quantum defect, broad and smooth emission cross section, and favorable thermo-optic properties [35,45]. Pulses as short as 30 fs have been demonstrated via this laser crystal in Kerr-lens modelocked oscillators [46]. The specific properties of the crystal relevant to this work are summarized in Table 3. A polarizing beam splitter is used to split the laser output from the incident pump beam (Fig. 1). Therefore, the incident pump is horizontally polarized while the output laser light must be vertically polarized. The c-axis of the Yb:CALGO is oriented in the horizontal, yielding maximum absorption for the horizontally polarized pump light (σ-polarization) and maximum gain for the vertically polarized laser light (π-polarization) [47].

Table 3. Relevant gain material parameters used for the straight cavity design.

Gain material properties	
Gain crystal	Yb:CaGdAlO$_4$ (Yb:CALGO)
Crystallographic orientation	a-cut
Aperture	4×1 mm^2
Crystal length	1.5 mm
Doping concentration (in melt)	5 at% (6.25×10^{20} / cm^3)
Dispersion @ 1040 nm	108 fs^2/ mm [20]
Nonlinear index coefficient n_2	$n_2 = 9 \cdot 10^{-20}$ m^2/W [48]

Output coupler

The mode sizes on the different intracavity elements are important parameters in a straight-cavity design. They are influenced by the curvature of the output coupler and the placement of the components. Performance parameters like the optical-to-optical slope efficiency, lasing threshold and single transverse mode operation depend on the cavity mode size in the gain crystal and its overlap with the pump mode. The mode size in the PPLN crystal and on the SESAM strongly influence the modelocking dynamics by determining the amount of generated SPM, nonlinear losses of the cascading process as well as the non-saturated losses introduced by the SESAM. In Fig. 10, we show the 1/e^2 mode radius, calculated with the ABCD-matrix formalism for Gaussian beams, within the cavity for three tested laser configurations with varying OC curvatures. For each mirror curvature, the placement of the cavity components was adjusted to keep the mode size in the gain crystal constant to maintain matching to the pump mode.
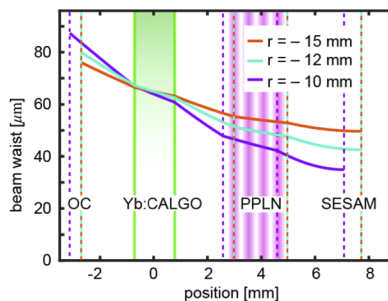

Fig. 10. Beam waist inside the "cold" cavity (i.e. at zero Kerr-lens) as a function of the position of the cavity elements for 3 different curvatures of the second cavity mirror. The zero point was chosen in the center of the Yb:CALGO crystal.

We observed modelocking for all three mirror curvatures and found that 12 mm yielded the best performance. The corresponding trade-offs are discussed further in Appendix B.

Appendix B: Trade-offs involved in modelocked operation

The influence of various processes and the resulting trade-offs determine the limits of modelocking performance. These issues can best be demonstrated using the experimental data shown in Fig. 11: in Fig. 11(a), we show the output power slope as a function of pump power, while Fig. 11(b) shows the corresponding spectra recorded with an optical spectrum analyzer for a laser configuration using a curved mirror with a radius of curvature of 10 mm and an OC-coating with a GDD of -550 fs^2 at a wavelength of 1045 nm (summarized in Table 4). As a result of the smaller mirror radius of curvature (10 mm instead of 12 mm), the mode sizes are smaller in the PPLN and on the SESAM, but are kept the same in the gain crystal (Fig. 3). The smaller mode sizes lead to more SPM in the PPLN and a stronger saturation of the SESAM for a given intracavity average power. Hence, the cw-modelocking threshold is relatively low ($\sim$380 mW). From soliton modelocking theory [38], one would expect the pulse duration to be inversely proportional to the pulse energy. We observe qualitatively similar behavior: with increasing average power, the pulse duration decreases and the spectrum broadens. However, we also observe a significant self-frequency shift (SFS), i.e. a shift of the center wavelength towards shorter wavelengths (Fig. 11(b)). SFS effects were first observed in single-pass CQN devices, with analogies to the Raman soliton SFS [43], but here the process occurs intracavity. One can understand this effect as follows: the long wavelength part of the laser spectrum is closer to phase matching, which increases the amount of energy transferred to the weakly excited second harmonic. This weak second-harmonic component represents a loss to the fundamental laser wavelength. As the spectrum broadens with increased pump power, the laser wavelength shifts to shorter wavelengths in order to minimize this additional loss. The induced SFS of the spectrum in Fig. 11(b) amounts to -4.6 nm/W and occurs up to an output power of 1 W. Beyond that power, we observe a distortion of the output beam (Fig. 11(a), inset). The spectrum does not broaden anymore and the pulse duration remains constant, even though the output power increases up to a maximum value of 1.32 W.
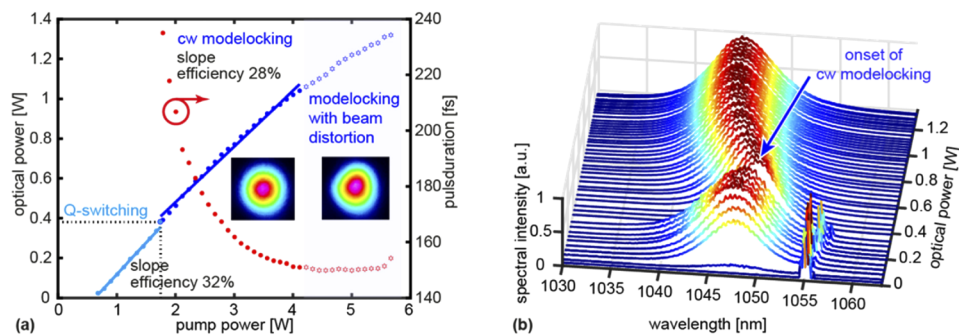

Fig. 11. Modelocking characterization for the configuration with mirror curvature of 10 mm. (a) Measured optical power from lasing threshold up to a maximum output power of 1.32 W (blue dots) and the corresponding measured pulse duration in the cw-modelocking regime. (b) Normalized optical spectrum measured over the entire range of output powers.

The strong Kerr-lens defocusing effect caused by the small beam waist in the PPLN offers better protection during Q-switching instability below the cw-modelocking threshold, but also leads to a strong SFS, which ultimately limits the achievable pulse duration. In addition, we typically observe a greater tendency for beam distortions at high powers when operating the laser in configurations with a large SFS coefficient. Hence, reducing the mode size in the PPLN

Table 4. Laser configuration for the investigation of the limitations of modelocking performance.

Laser parameters		
Mirror curvature	10 mm	15 mm
Output coupling rate	2.6% @ 1045 nm	2.6% @ 1045 nm
Group delay dispersion output coupler (GDD_{OC})	-550 fs^2	-550 fs^2
Total group delay dispersion (GDD_{tot})	730 fs^2	730 fs^2
PPLN grating vector K_g	908.4 mm^{-1}	914.8 mm^{-1}
Repetition rate f_{rep}	10.69 GHz	10.50 GHz
Cw-modelocking threshold	380 mW	498 mW
Maximum average power P_{avg} (max. P_{avg} with distortion)	1.0 W (1.32 W)	981 mW
Pulse duration τ_p	150 fs	167 fs
Center wavelength λ_0	1045 nm	1044 nm
Spectral bandwidth (FWHM) $\Delta\lambda$	7.7 nm	7.1 nm
Modelocking slope efficiency	28%	31%

to enhance the SPM did not yield significantly shorter pulse durations. Optimization of the cavity GDD has proven to be a more successful approach to obtaining shorter pulses, as we demonstrated in Section 2.4.

We have also used an output coupler with the same thin-film coating, but with a larger radius of curvature of 15 mm. We observed a greater tendency for modelocking instabilities which required operating closer to phase matching in order to clamp the intracavity intensity. As a result, we observed a lower output power compared to the configuration with a 10 mm curvature. The achieved performance is summarized in Table 4. We used a 12-mm radius of curvature for the results presented in the main text.

Disclosures

The authors declare no conflicts of interest.

References

1. H. R. Telle, G. Steinmeyer, A. E. Dunlop, J. Stenger, D. H. Sutter, and U. Keller, "Carrier-envelope offset phase control: A novel concept for absolute optical frequency measurement and ultrashort pulse generation," Appl. Phys. B **69**(4), 327–332 (1999).
2. D. J. Jones, S. A. Diddams, J. K. Ranka, A. Stentz, R. S. Windeler, J. L. Hall, and S. T. Cundiff, "Carrier-Envelope Phase Control of Femtosecond Mode-Locked Lasers and Direct Optical Frequency Synthesis," Science **288**(5466), 635–639 (2000).
3. A. Apolonski, A. Poppe, G. Tempea, Ch. Spielmann, Th. Udem, R. Holzwarth, T. W. Hänsch, and F. Krausz, "Controlling the Phase Evolution of Few-Cycle Light Pulses," Phys. Rev. Lett. **85**(4), 740–743 (2000).
4. S. Schiller, "Spectrometry with frequency combs," Opt. Lett. **27**(9), 766 (2002).
5. I. Coddington, N. Newbury, and W. Swann, "Dual-comb spectroscopy," Optica **3**(4), 414–426 (2016).

6. S. M. Link, D. J. H. C. Maas, D. Waldburger, and U. Keller, "Dual-comb spectroscopy of water vapor with a free-running semiconductor disk laser," Science **356**(6343), 1164–1168 (2017).
7. J. Nürnberg, C. G. E. Alfieri, Z. Chen, D. Waldburger, N. Picqué, and U. Keller, "An unstabilized femtosecond semiconductor laser for dual-comb spectroscopy of acetylene," Opt. Express **27**(3), 3190 (2019).
8. A. Jallageas, J. Nürnberg, C. G. E. Alfieri, C. G. E. Alfieri, D. Waldburger, S. M. Link, F. Emaury, F. Emaury, J. Morel, and U. Keller, "Calibration of high-accuracy spectrometers using stabilized 11-GHz femtosecond semiconductor laser," Opt. Express **27**(26), 37552–37558 (2019).
9. M. Endo, T. D. Shoji, and T. R. Schibli, "Ultralow Noise Optical Frequency Combs," IEEE J. Sel. Top. Quantum Electron. **24**(5), 1–13 (2018).
10. V. Torres-Company, J. Schröder, A. Fülöp, M. Mazur, L. Lundberg, Ó. B. Helgason, M. Karlsson, and P. A. Andrekson, "Laser Frequency Combs for Coherent Optical Communications," J. Lightwave Technol. **37**(7), 1663–1670 (2019).
11. M.-G. Suh and K. J. Vahala, "Soliton microcomb range measurement," Science **359**(6378), 884–887 (2018).
12. P. Trocha, M. Karpov, D. Ganin, M. H. P. Pfeiffer, A. Kordts, S. Wolf, J. Krockenberger, P. Marin-Palomo, C. Weimann, S. Randel, W. Freude, T. J. Kippenberg, and C. Koos, "Ultrafast optical ranging using microresonator soliton frequency combs," Science **359**(6378), 887–891 (2018).
13. R. A. McCracken, J. M. Charsley, and D. T. Reid, "A decade of astrocombs: recent advances in frequency combs for astronomy [Invited]," Opt. Express **25**(13), 15058–15078 (2017).
14. C. Kerse, H. Kalaycıoğlu, P. Elahi, B. Çetin, D. K. Kesim, Ö Akçaalan, S. Yavaş, M. D. Aşık, B. Öktem, H. Hoogland, R. Holzwarth, and FÖ Ilday, "Ablation-cooled material removal with ultrafast bursts of pulses," Nature **537**(7618), 84–88 (2016).
15. R. Paschotta, L. Krainer, S. Lecomte, G. J. Spühler, S. C. Zeller, A. Aschwanden, D. Lorenser, H. J. Unold, K. J. Weingarten, and U. Keller, "Picosecond pulse sources with multi-GHz repetition rates and high output power," New J. Phys. **6**, 174 (2004).
16. G. J. Spühler, L. Krainer, S. C. Zeller, C. Erny, R. Paschotta, K. J. Weingarten, and U. Keller, "Compact low-noise pulse generating lasers with repetition rates of 10 to 50 GHz," Int. J. High Speed Electron. Syst. **15**(03), 497–512 (2005).
17. A. Bartels, D. Heinecke, and S. A. Diddams, "Passively mode-locked 10 GHz femtosecond Ti:sapphire laser," Opt. Lett. **33**(16), 1905–1907 (2008).
18. M. Endo, I. Ito, and Y. Kobayashi, "Direct 15-GHz mode-spacing optical frequency comb with a Kerr-lens mode-locked $Yb:Y_2O_3$ ceramic laser," Opt. Express **23**(2), 1276–1282 (2015).
19. H.-W. Chen, G. Chang, S. Xu, Z. Yang, and F. X. Kärtner, "3 GHz, fundamentally mode-locked, femtosecond Yb-fiber laser," Opt. Lett. **37**(17), 3522–3524 (2012).
20. A. Klenner, M. Golling, and U. Keller, "High peak power gigahertz Yb:CALGO laser," Opt. Express **22**(10), 11884 (2014).
21. S. Kimura, S. Tani, and Y. Kobayashi, "Kerr-lens mode locking above a 20 GHz repetition rate," Optica **6**(5), 532 (2019).
22. M. Mangold, C. A. Zaugg, S. M. Link, M. Golling, B. W. Tilma, and U. Keller, "Pulse repetition rate scaling from 5 to 100 GHz with a high-power semiconductor disk laser," Opt. Express **22**(5), 6099–6107 (2014).
23. D. Waldburger, A. S. Mayer, C. G. E. Alfieri, J. Nürnberg, A. R. Johnson, X. Ji, A. Klenner, Y. Okawachi, M. Lipson, A. L. Gaeta, and U. Keller, "Tightly locked optical frequency comb from a semiconductor disk laser," Opt. Express **27**(3), 1786 (2019).
24. T. J. Kippenberg, A. L. Gaeta, M. Lipson, and M. L. Gorodetsky, "Dissipative Kerr solitons in optical microresonators," Science **361**(6402), eaan8083 (2018).
25. D. R. Carlson, D. D. Hickstein, W. Zhang, A. J. Metcalf, F. Quinlan, S. A. Diddams, and S. B. Papp, "Ultrafast electro-optic light with subcycle control," Science **361**(6409), 1358–1363 (2018).
26. T. Steinmetz, T. Wilken, C. Araujo-Hauck, R. Holzwarth, T. W. Hänsch, and T. Udem, "Fabry–Pérot filter cavities for wide-spaced frequency combs with large spectral bandwidth," Appl. Phys. B **96**(2-3), 251–256 (2009).
27. D. N. Christodoulides, I. C. Khoo, G. J. Salamo, G. I. Stegeman, and E. W. Van Stryland, "Nonlinear refraction and absorption: mechanisms and magnitudes," Adv. Opt. Photonics **2**(1), 60 (2010).
28. C. Hönninger, R. Paschotta, F. Morier-Genoud, M. Moser, and U. Keller, "Q-switching stability limits of continuous-wave passive mode locking," J. Opt. Soc. Am. B **16**(1), 46–56 (1999).
29. A. Klenner and U. Keller, "All-optical Q-switching limiter for high-power gigahertz modelocked diode-pumped solid-state lasers," Opt. Express **23**(7), 8532 (2015).
30. A. S. Mayer, C. R. Phillips, and U. Keller, "Watt-level 10-gigahertz solid-state laser enabled by self-defocusing nonlinearities in an aperiodically poled crystal," Nat. Commun. **8**(1), 1673 (2017).
31. U. Keller, K. J. Weingarten, F. X. Kartner, D. Kopf, B. Braun, I. D. Jung, R. Fluck, C. Honninger, N. Matuschek, and J. Aus der Au, "Semiconductor saturable absorber mirrors (SESAM's) for femtosecond to nanosecond pulse generation in solid-state lasers," IEEE J. Sel. Top. Quantum Electron. **2**(3), 435–453 (1996).
32. C. R. Phillips, A. S. Mayer, A. Klenner, and U. Keller, "Femtosecond mode locking based on adiabatic excitation of quadratic solitons," Optica **2**(8), 667 (2015).
33. A. R. Johnson, A. S. Mayer, A. Klenner, K. Luke, E. S. Lamb, M. R. E. Lamont, C. Joshi, Y. Okawachi, F. W. Wise, M. Lipson, U. Keller, and A. L. Gaeta, "Octave-spanning coherent supercontinuum generation in a silicon nitride waveguide," Opt. Lett. **40**(21), 5117–5120 (2015).

34. K. R. Parameswaran, R. K. Route, J. R. Kurz, R. V. Roussev, M. M. Fejer, and M. Fujimura, "Highly efficient second-harmonic generation in buried waveguides formed by annealed and reverse proton exchange in periodically poled lithium niobate," Opt. Lett. **27**(3), 179–181 (2002).

35. J. Petit, P. Goldner, and B. Viana, "Laser emission with low quantum defect in Yb:CaGdAlO₄," Opt. Lett. **30**(11), 1345 (2005).

36. G. I. Stegeman, D. J. Hagan, and L. Torner, "$\chi^{(2)}$ cascading phenomena and their applications to all-optical signal processing, mode-locking, pulse compression and solitons," Opt. Quantum Electron. **28**(12), 1691–1740 (1996).

37. O. Gayer, Z. Sacks, E. Galun, and A. Arie, "Temperature and wavelength dependent refractive index equations for MgO-doped congruent and stoichiometric LiNbO₃," Appl. Phys. B **91**(2), 343–348 (2008).

38. F. X. Kärtner, I. D. Jung, and U. Keller, "Soliton mode-locking with saturable absorbers," IEEE J. Sel. Top. Quantum Electron. **2**(3), 540–556 (1996).

39. A. E. Siegman, "New developments in laser resonators," Proc. SPIE **1224**, 2 (1990).

40. C. R. Phillips, J. S. Pelc, and M. M. Fejer, "Parametric processes in quasi-phasematching gratings with random duty cycle errors," J. Opt. Soc. Am. B **30**(4), 982–993 (2013).

41. R. Paschotta, "Beam quality deterioration of lasers caused by intracavity beam distortions," Opt. Express **14**(13), 6069–6074 (2006).

42. A. E. H. Oehler, M. C. Stumpf, S. Pekarek, T. Südmeyer, K. J. Weingarten, and U. Keller, "Picosecond diode-pumped 1.5 μm Er,Yb:glass lasers operating at 10–100 GHz repetition rate," Appl. Phys. B **99**(1-2), 53–62 (2010).

43. FÖ Ilday, K. Beckwitt, Y.-F. Chen, H. Lim, and F. W. Wise, "Controllable Raman-like nonlinearities from nonstationary, cascaded quadratic processes," J. Opt. Soc. Am. B **21**(2), 376 (2004).

44. U. Keller and A. C. Tropper, "Passively modelocked surface-emitting semiconductor lasers," Phys. Rep. **429**(2), 67–120 (2006).

45. P. Loiko, F. Druon, P. Georges, B. Viana, and K. Yumashev, "Thermo-optic characterization of Yb:CaGdAlO₄ laser crystal," Opt. Mater. Express **4**(11), 2241–2249 (2014).

46. N. Modsching, C. Paradis, F. Labaye, M. Gaponenko, I. J. Graumann, A. Diebold, F. Emaury, V. J. Wittwer, and T. Südmeyer, "Kerr lens mode-locked Yb:CALGO thin-disk laser," Opt. Lett. **43**(4), 879 (2018).

47. K. Hasse, T. Calmano, B. Deppe, C. Liebald, and C. Kränkel, "Efficient Yb⁺³:CaGdAlO₄ bulk and femtosecond-laser-written waveguide lasers," Opt. Lett. **40**(15), 3552 (2015).

48. J. Boudeile, F. Druon, M. Hanna, P. Georges, Y. Zaouter, E. Cormier, J. Petit, P. Goldner, and B. Viana, "Continuous-wave and femtosecond laser operation of Yb:CaGdAlO₄ under high-power diode pumping," Opt. Lett. **32**(14), 1962 (2007).